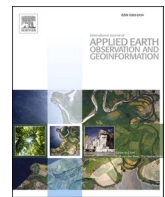


Contents lists available at ScienceDirect

International Journal of Applied Earth Observations and Geoinformation

journal homepage: www.elsevier.com/locate/jag



Comprehensively analyzing optical and polarimetric SAR features for land-use/land-cover classification and urban vegetation extraction in highly-dense urban area

Yunkun Bai ^{a,e,f}, Guangmin Sun ^a, Yu Li ^{a,*}, Peifeng Ma ^b, Gang Li ^c, Yuanzhi Zhang ^{d,*}

^a Faculty of Information Technology, Beijing University of Technology, Beijing 100124, China

^b Institute of Space and Earth Information Science, the Chinese University of Hong Kong, Hong Kong, China

^c School of Geospatial Engineering and Science, Sun Yat-Sen University, Zhuhai, China

^d National Observatory, Chinese Academy of Sciences, Beijing 100101, China

^e Key Laboratory of Particle & Radiation Imaging (Tsinghua University), Ministry of Education, China

^f Department of Engineering Physics, Tsinghua University, Beijing 100084, China



ARTICLE INFO

Keywords:

Synthetic Aperture Radar
Optical Remote Sensing
Urban Land-Use and Land-Cover
Vegetation
Image Classification

ABSTRACT

Vegetation is a land-use type that attracting growing attention in urban studies. Extraction of urban vegetation information can be achieved by land-use/land-cover (LULC) classification. It has been proved that SAR remote sensing provides complementary information in LULC classification. However, how the complementary information from SAR features contribute to the classification in highly-dense urban area is still unclear. In this study, taking the highly urbanized area of Hong Kong as the study site, comprehensive studies were conducted to investigate the contribution of optical and polarimetric SAR features for LULC classification and urban vegetation extraction. Firstly, large amount of redundant information was found within optical and SAR features sets by Pearson correlation analysis. Then analysis based on J-S distance revealed that optical features have much stronger capabilities on LULC classification and some key features such as NDVI and Mean value of GLCM carry distinct information for discriminating certain land-use types. Supervised classification based on random forest further proved this result. The complementary mechanism of optical and polarimetric SAR features can be clearly observed in the radar chart. Therefore, when fusing optical and SAR features on the feature-level, the classification accuracy further improved. It was discovered that the volume scatter mechanism plays a vital role in the feature-level classification model. Finally, the overall classification accuracy of the classification model does not significantly grow after several key optical and SAR features are inputted, confirming again the high correlation between the features. In vegetation extraction, optical features provide most information and achieved the high accuracy of 99.02%. The results discovered in the above research could benefit the designing algorithms and selecting features for high accuracy urban LULC classification and vegetation extraction based on optical and SAR data.

1. Introduction

Urban vegetation is very significant component of the urban environment. It plays a key role in ecological, public health and psychological aspects by reducing air pollution, purifying water, sterilization, supplementing oxygen, reducing noise, preventing soil and water loss and providing comment space for exercise and recreation activities (Kang et al., 2020; Zhang et al., 2018a). Represented as vegetation in remote sensing images, urban green spaces such as parks, forests and green belts

can also reduce the urban heat island effect and increasing air moisture, providing huge benefits to the urban residence (Kuang and Dou, 2020). Accurate and timely monitoring the distribution of urban vegetation is important for the planning, construction and management for urban ecological environment (Kang et al., 2020; Zhang et al., 2018a; Kuang and Dou, 2020).

The accurate mapping of urban vegetation relies on the high-quality classification of land-use and land-cover. At earlier stage, studies are mainly focused on remote sensing applications based on optical sensors

* Corresponding authors.

E-mail addresses: yuli@bjut.edu.cn (Y. Li), zhangyz@nao.cas.cn (Y. Zhang).

(Ridd, 1995; Wu and Murray, 2003; Weng et al., 2008). Spectral confusion (same types of targets having different spectrums; same spectrum characteristics shared by different types of targets) and shade effect (variations of lighting conditions caused by topography or tall building blocks and clouds) are two main factors that affect the accuracy land-use and land-cover classification (Deng and Wu, 2012; Lu and Weng, 2006).

As an active remote sensing device, synthetic aperture radar (SAR) is not vulnerable to adverse light and weather conditions (Chen et al., 2011). Different with optical sensors, it measures the dielectric and geometric properties of the ground target (Li et al., 2013; Zhang et al., 2012b; Zhang et al., 2012a). As a result, SAR could provide key complementary information for optical sensors (Henderson and Xia, 1997; Zhang et al., 2015; Salentini and Gamba, 2015). Polarimetric SAR (Pol-SAR) measures the scattering behavior of ground target under various transmission and receiving polarization status, which could provide extra information in distinguishing different land-use types (Bhattacharya and Touzi, 2011; Lee and Pottier, 2017; Dare, 2005). Moreover, a synergic approach that uses optical and radar satellite measurements can also achieve a denser temporal coverage of the area of interest. There are cities where the cloud cover is dominant during the year and therefore if structural urbanistic changes occur, they can be missed by using optical sensor only.

In recent years, interests are growing on the study of land-cover classification based on fusing optical and SAR images. The fusion can be performed on three different levels, namely, pixel level, features level and decision level (Schmitt and Zhu, 2016; Zhang et al., 2017). Pixel level fusion between optical and SAR sensors usually does not have satisfying result, because the imaging mechanism between these two sensors is totally different. Artificial neural network, support vector machine, decision tree and ensemble learning methods that combine different classifiers were proposed for feature-level fusion of optical and SAR data (Lim et al., 2000; Rokach, 2010), which achieved some promising results. Decision level fusion such as majority voting, entropy weighting and Dempster-Shafer theory also demonstrated their potential in urban land-use classification (Kang et al., 2020; Kuang and Dou, 2020).

However, challenges remain in this research field. Firstly, the contribution of optical and Pol-SAR features in higher spatial-resolution (less than 10 m) images has not been synergistically analyzed. Hence the mechanism of how the Pol-SAR and optical features can be better fused need to be further explored. Moreover, since many features can be extracted from optical and SAR data, the selection and optimization of the feature set need to be better investigated.

In this paper, comprehensive studies were conducted on high-resolution images less than 10 m resolution. The rest part of this paper is arranged as follows: in Section 2, basic methodology of the proposed study is introduced. In Section 3, experimental results on the study site are introduced. Then in Section 4, discussions on the experimental results are provided. Finally, in Section 5, a brief conclusion is made.

2. Methodology

2.1. Optical features extraction

In order to fully take the advantage of multispectral information obtained from the optical image, features from the perspective of HSV color space, key indexes and texture properties were extracted in this study.

2.1.1. HSV color space features

The HSV color space has three components: hue, saturation and value. Compared with Red, Green and Blue (RGB) color space, the HSV color space is more similar to the way in which humans perceive color, and it can be converted directly from RGB color space by:

Table 1

Optical features considered for this study.

Features	Descriptions
GF-blue	Bands of GF-1 image: Blue;
GF-green	Green;
GF-red	Red;
GF-NIR	Near infra-red
HSV-H	HSV color space features: Hue;
HSV-S	Saturation;
HSV-V	Value
NDWI	Normalized Difference Water Index
NDVI	Normalized Difference Vegetation Index
Mean value	GLCM texture features of Pan band
Variance	
Angular second moment(ASM)	
Homogeneity	
Contrast;	
Dissimilarity	
Entropy	

$$H = \begin{cases} \cos^{-1} \left\{ \frac{(R - G) + (R - B)}{\sqrt[3]{(R - G)^2 + (R - B)(G - B)}} \right\} & \text{if } (B \leq G) \\ 360^\circ - \cos^{-1} \left\{ \frac{(R - G) + (R - B)}{\sqrt[3]{(R - G)^2 + (R - B)(G - B)}} \right\} & \text{if } (B > G) \end{cases} \quad (1)$$

$$S = \frac{\max(R, G, B) - \min(R, G, B)}{\max(R, G, B)} \quad (2)$$

$$V = \frac{\max(R, G, B)}{255} \quad (3)$$

The value of H is within [0,360] and S , V is within [0,1].

2.1.2. Normalized difference vegetation index (NDVI)

NDVI is a largely used indicator for vegetation coverage. It increases with the growth of vegetation density and could avoid the affection of irradiance change to a certain extent.

$$NDVI = \frac{NIR - Red}{NIR + Red} \quad (4)$$

where Red and NIR stand for the spectral reflectance of red and near-infrared bands, respectively.

2.1.3. Normalized difference water index (NDWI)

NDWI was proposed to highlight the water area in optical images:

$$NDWI = (Green - NIR)/(Green + NIR) \quad (5)$$

NDWI takes advantage of the higher reflectance of water at shorter wavelength and lower reflectance at longer wavelength.

2.1.4. Texture features

In this paper, the gray level co-occurrence matrix(GLCM) of GF-1 panchromatic band is used to extract the texture information. GLCM is defied over an image by counting the number of co-occurring pixel grayscale at a given offset. A window size of 7×7 pixels is used for the calculation of CLCM. Four texture measures that derived from the GLCM are taken as texture features: Mean, Variance, Homogeneity(HOM), Contrast, Dissimilarity (DISS), Entropy (ENT) and the Angular second moment (ASM) (Shao et al., 2016), their the efficiency on describing texture behavior of ground targets in urban area have been proved: HOM measures the homogeneity of the image; DISS linearly increases when the difference of local pixel pair grows; ASM is large when the variation of the image is regular; ENT reflects the randomness of the

Table 2
Polarimetric SAR features considered for this study.

Features		Descriptions
Alpha Entropy	$\text{Alpha} = P_1\alpha_1 + P_2\alpha_2 + P_3\alpha_3$	Average polarimetric angle
Anisotropy	$\text{Entropy} = -\sum_{i=1}^3 P_i \log P_i$	Polarimetric Entropy
	$\text{Anisotropy} = \frac{\lambda_2 - \lambda_3}{\lambda_2 + \lambda_3}$	Anisotropy(Cloude-Pottier decomposition)
Krogager_Ks(k_s)	$S = e^{j\varphi} \{e^{j\varphi_s} k_s S_S + k_d S_D + k_h S_H\}$	Single scattering contribution,
Krogager_Kd(k_d)		Double scattering contribution,
Krogager_Kh(k_h)		Helical scattering contribution (Krogager decomposition)
Freeman_Odd(f_s)	$\langle [C] \rangle = f_s[C_S] + f_D[C_D] + f_V[C_V]$	Surface scattering,
Freeman_Dbl(f_D)		Double bounce Scattering and Volume scattering components (Freeman decomposition)
Freeman_Vol(f_V)		(Freeman decomposition)
VanZyl_Odd(f_s)	$\langle [C] \rangle = f_s[C_S] + f_D[C_D] + f_V[C_V]$	Surface scattering,
VanZyl_Dbl(f_D)	$+ f_V[C_V] + [C_{\text{reminder}}]$	Double bounce Scattering and Volume scattering components (VanZyl decomposition)
VanZyl_Vol(f_V)		(VanZyl decomposition)
Yamaguchi_Odd(f_s)	$\langle [C] \rangle = f_s[C_S] + f_D[C_D] + f_V[C_V]$	Surface scattering,
Yamaguchi_Dbl(f_D)	$+ f_C[C_C]$	Double bounce Scattering and Volume scattering components
Yamaguchi_Vol(f_V)		helix components (Yamaguchi decomposition)
Yamaguchi_Hlxl(f_C)		
T_{11}, T_{22}, T_{33}	$T = \begin{pmatrix} T_{11} & T_{12} & T_{13} \\ T_{21} & T_{22} & T_{23} \\ T_{31} & T_{32} & T_{33} \end{pmatrix}$	Coherence coefficients derived from coherence matrix

textures of the image.

The optical features considered for this study are summarized in Table 1.

2.2. Polarimetric features extraction

Polarimetric SAR system transmit and receive the radar signal under various polarization basis, in which way the scattering mechanism of the ground target can be better obtained. In this study, three key elements of coherence matrix T derived from quad-polarimetric SAR data were considered. Moreover, polarimetric decompositions were proposed to better explore physical properties of the target from the polarimetric SAR data. Krogager decomposition was proposed by transforming the scatter matrix S of any complex, symmetric radar target by a rotation operator R , and decompose S into three components that caused by sphere, oriented diplane and helix (Krogager, 1990). Cloude et al. conducted eigenvalues analysis on the coherence matrix of polarimetric SAR data, and derived Entropy H, Anisotropy A and average scattering angle α to quantitatively describe the scatter behavior SAR backscatter (Cloude and Pottier, 1997). Freeman decomposition was proposed to describe the polarimetric backscatter from naturally occurring scatters (Freeman and Durden, 1998). It could decompose the covariance matrix of polarimetric SAR data into components from surface, double bounce and volume scatters based on physical model. Yamaguchi et al., further improved the Freeman decomposition by introducing helix component to represent the co-pol and the cross-pol correlations in complex urban area (Yamaguchi et al., 2005). In order to solve the problem of negative scattering components suffered by the model-based decomposition models, Van Zyl et al. proposed a modification to ensure that all covariance matrices in the decomposing will be none-negative by combine model-based decomposition with eigenvector decomposition (Van Zyl et al., 2008). Moreover, there is a special polarimetric mode

used by CosmoSkyMed SARs which is known as Ping-Pong. In this case the polarimetric is dual but not coherent, and the time difference between the two polarimetric acquisition can be exploited to discriminate between marine, vegetated and urban built areas (Migliaccio et al., 2014).

In this study, polarimetric SAR features were extracted from the polarimetric SAR data. These features and their brief definition are shown in Table 2.

2.3. Statistical analysis tools

As two remote sensing observation methods with completely different imaging mechanisms, optical remote sensing and SAR can obtain complementary information that helps land-use/land-cover classification. Therefore, how to select features that contain these complementary information is the key to LULC classification and urban vegetation extraction. This paper analyzes and evaluates features from the following three aspects: the correlation between features, the separability of features between different categories, and the contribution of features to classification results. Based on the results of feature analysis, appropriate features can be selected for LULC classification and vegetation extraction.

2.3.1. Pearson correlation coefficients

Feature correlation analysis is to measure the redundant information between two features. Pearson correlation coefficients are a decent measure of the linear correlation within variables. Therefore, the Pearson correlation coefficients are calculated separately for optical features and SAR features to analyze the correlation between features. The Pearson correlation coefficients between two variables are defined as the quotient of the covariance and standard deviation between the two variables:

$$\rho_{X,Y} = \frac{\text{cov}(X, Y)}{\sigma_X \sigma_Y} \quad (6)$$

Among them, $\text{cov}(X, Y)$ represents the covariance of X and Y . σ_X, σ_Y represent the standard deviation of sample X and Y respectively. We can calculate the covariance and standard deviation of the sample to derive the sample correlation coefficient r :

$$r = \frac{\sum_{k=0}^n (X_i - \bar{X})(Y_i - \bar{Y})}{\sqrt{\sum_{k=0}^n (X_i - \bar{X})^2} \sqrt{\sum_{k=0}^n (Y_i - \bar{Y})^2}} \quad (7)$$

where \bar{X} and \bar{Y} are the average values of samples of X and Y , and n is the number of samples.

2.3.2. Measurement of separability

In order to quantitatively analyze the capability of the above introduced features in distinguishing different land-use types, statistical analysis was applied.

Kullback–Leibler (K-L) divergence is widely used to quantitatively measure the capability of features in distinguishing different kinds of ground targets.

K-L divergence is also called relative entropy, it measures how a probability distribution diverges from another expected probability distribution.

Given two possibility distribution functions (PDF), the entropy and cross entropy is calculated as:

$$H(p) = \sum p(x) \log \frac{1}{p(x)} \quad (8)$$

$$H(p, q) = \sum p(x) \log \frac{1}{q(x)} \quad (9)$$

Then the K-L divergence:

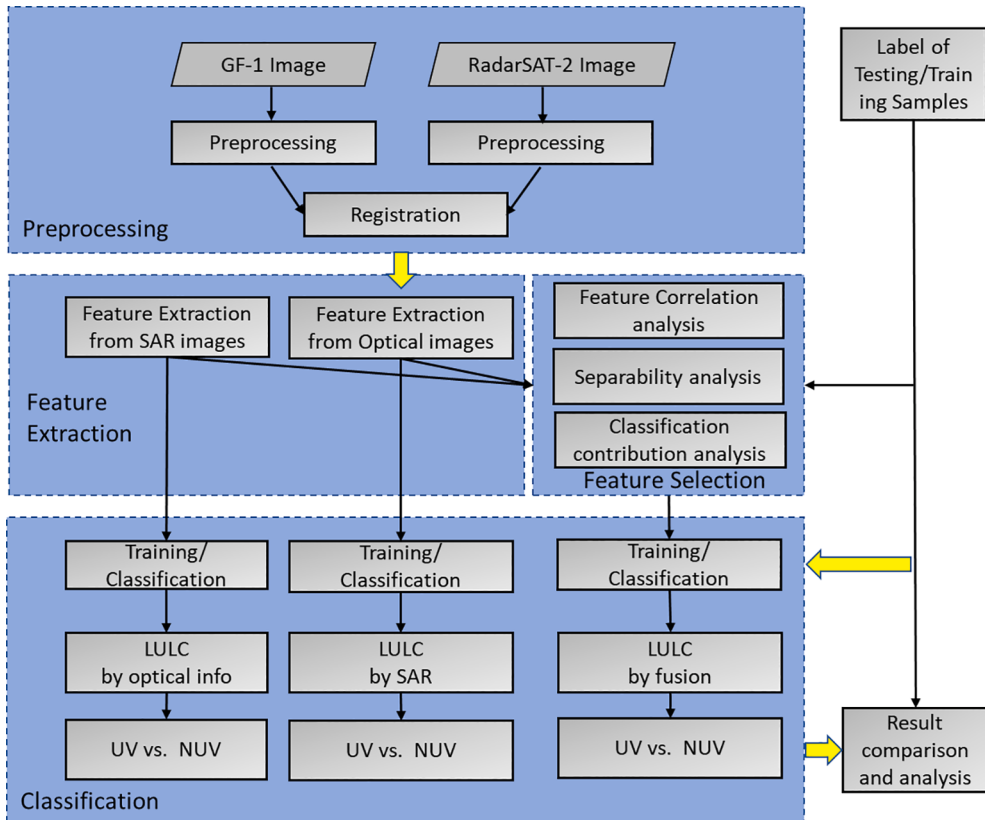


Fig. 1. The flowchart of the study.

$$D(p\|q) = H(p) - H(p, q) = \sum p(x) \log \frac{p(x)}{q(x)} \quad (10)$$

K-L divergence gets larger when $p(x)$ and $q(x)$ is more differently distributed and become 0 when the two distributions are identical.

However, the K-L divergence $D(p\|q)$ and $D(q\|p)$ are not necessarily to be identical. As the result, in this study, the J-S(Jensen-Shannon) distance, a variant of K-L divergence, was used to evaluate the separability of two distributions. J-S divergence is symmetrical, and its value is between 0 and 1. The definition is as follows:

$$JS(p, q) = D\left(p\left\|\frac{p+q}{2}\right.\right)/2 + D\left(q\left\|\frac{p+q}{2}\right.\right)/2 \quad (11)$$

2.4. Supervised classifier

It is crucial to understand the contribution and interaction of features when fusing optical and polarimetric SAR data for land-use/land-cover classification. Although recent classifiers such as neural network achieved good performance in land-use classification for their high non-linear fitting capabilities, they usually work as “black box”, and does not help in understanding how the features are specifically used and interacted during the classification. One advantage of random forest(RF) algorithm is that it can output the contribution of each feature in the multi-feature classification model. Therefore, in this study, the random forest classifier was taken advantage to rank the contribution of each optical and polarimetric SAR features.

Random forest is a kind of ensemble learning algorithms. It was composed of several decision trees. The result of a random forest is voted by these decision trees. The optimum feature can be selected by impurity of separation results measured by Gini index.

The Gini index represents the probability that two randomly selected sample in the sample set belong to different classes, denoted as G . The formula for calculating the Gini index is:

$$G(p) = \sum_{k=1}^K p_k(1-p_k) = 1 - \sum_{k=1}^K p_k^2 \quad (12)$$

Among them, p_k represents the probability that the sample belongs to the k^{th} category.

Suppose there are m features: $X_1, X_2, X_3, \dots, X_m$. The importance of feature X_j at node m , the change in Gini index before and after the branch of node m is:

$$G_{jm} = G_m - G_l - G_r \quad (13)$$

Among them, G_l and G_r represent the Gini indices of the two new nodes after branching respectively.

If the feature X_j appears M times in the i^{th} tree, the importance of the feature X_j in the i^{th} tree is:

$$V_{ij} = \sum_{m=1}^M G_{jm} \quad (14)$$

The importance (contribution) of features to the classification is the average change in the impurity of the node splitting of the feature X_j in all trees in RF, which is defined as:

$$V_j = \frac{1}{n} \sum_{i=1}^n V_{ij} \quad (15)$$

Which n is the number of classification trees in RF.

2.5. Procedures of the experiment

The flowchart of the experiments in this study is shown in Fig. 1.

For GF-1 image, atmospheric correction, radiometric correction, geometric correction is applied. For RadarSAT-2 image, geometric and radiometric correction is conducted based on 10 m resolution Digital Elevation Model (DEM) data. Moreover, refined Lee filter is applied to

Table 3

The details of the data used for study.

Parameters/ Sensors	Gaofen-1	RadarSAT-2
Orbit Number	13,324	327,284
Acquisition Time	2015.10.16	2014.5.23
Resolution	about 8 m	about 8 m
Bands	Multi-spectrum: R, G, B, NIR	Quad-polarized SLC: HH, HV, VH, VV

alleviate the effect of speckle.

Optical and SAR images are geo-registered to UTM projection (zone 50 N) and WGS 84. Optical and SAR images are co-registered based on manually selected control points. Linear transformation approach is used for co-registration and the root mean square error (RMSE) for the image pair is less than one pixel.

Optical and SAR features are extracted respectively. The capability of features in distinguishing different kinds of ground targets are quantitatively measured by J-S divergence.

Taking the advantage of labeled training data samples, random forest was trained to classify ground targets into different land-use types

including: bright impervious surface (BIS), dark impervious surface (DIS), vegetation (VEG), bared soil (SOI) and water (WAT) (Zhang et al., 2018b). The training and testing data sets are randomly derived from the data sample and does not include each other to avoid data leakage.

Finally, ground targets are further clustered into urban vegetation (UV) and non-urban vegetation(NUV) by combining classification results of former step. Comprehensive analysis is conducted on land-use type classification as well as UV extraction results.

2.6. Accuracy assessment

Derived from the confusion matrix, overall accuracy (OA) and kappa coefficients (Kappa) are employed to quantitatively evaluate the classification accuracy. In confusion matrix, its rows represent the classified results and columns represent the referenced data. The last row is the sum of all previous rows, and the last column is the sum of all previous columns. The OA is calculated by summing the number of pixels classified correctly divided by the total number of pixels:

$$OA = \frac{\sum_{i=1}^{n-1} X_{ii}}{X_{nn}} \quad (16)$$

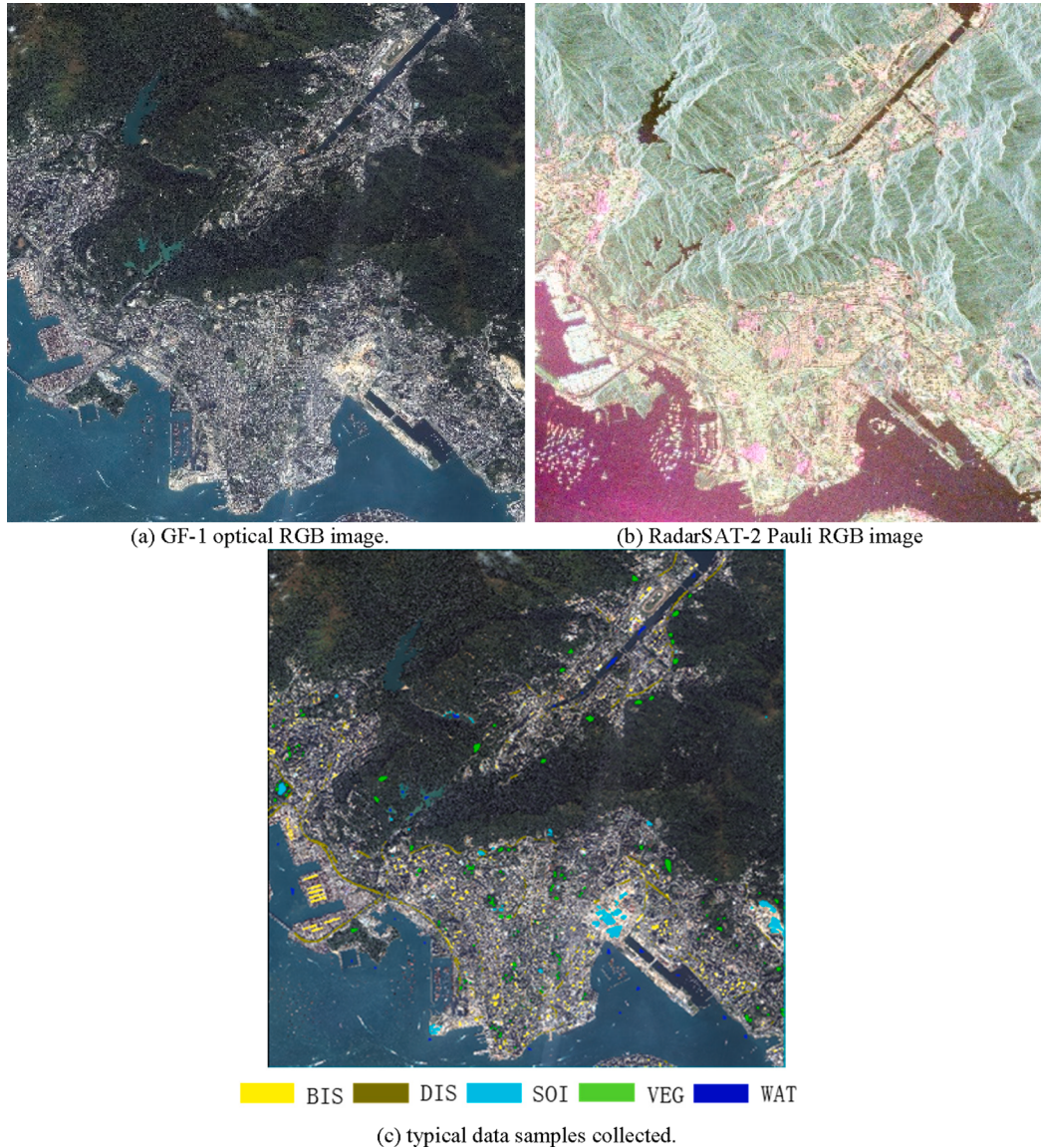


Fig. 2. Image of the study area.

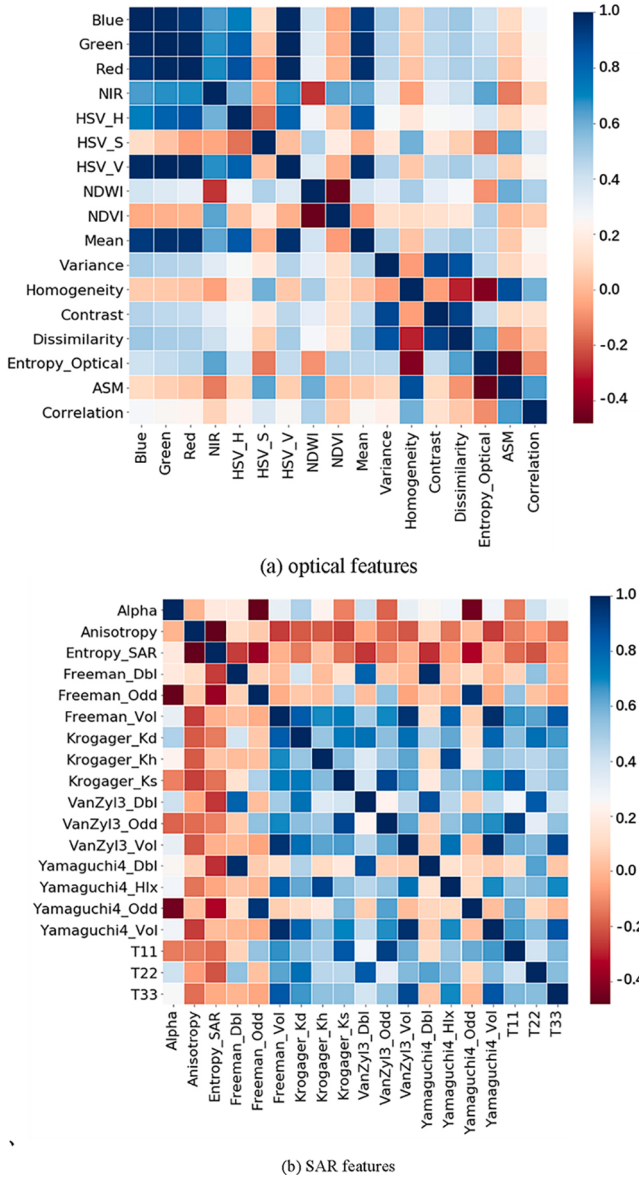


Fig. 3. Pearson correlation coefficient of (a) optical features, (b) SAR features.

Table 4
Separability analysis of optical features on distinguishing land-use and land-cover pairs.

Features	J-S divergence	BIS-DIS	BIS-SOI	BIS-VEG	BIS-WAT	DIS-SOI	DIS-VEG	DIS-WAT	SOI-VEG	SOI-WAT	VEG-WAT
Blue	0.4960	0.3261	0.6685	0.8983	0.6844	0.7502	0.9705	0.9792	0.9980	0.9980	0.6123
Green	0.4652	0.4462	0.7060	0.9249	0.8858	0.7495	0.9933	0.9980	0.9980	0.9980	0.5657
Red	0.4392	0.5289	0.7560	0.9511	0.9406	0.8099	0.9955	0.9965	0.9980	0.9980	0.5065
Nir	0.4302	0.4824	0.1545	0.8963	0.9376	0.5353	0.9808	0.3740	0.9980	0.9980	0.9980
HSV_H	0.9843	0.4783	0.6649	0.9582	0.9898	0.3739	0.9941	0.9980	0.9980	0.9980	0.5977
HSV_S	0.1374	0.3671	0.7569	0.8984	0.2453	0.7591	0.9980	0.8407	0.9361	0.9980	
HSV_V	0.4570	0.4705	0.7135	0.9386	0.8909	0.7783	0.9952	0.9980	0.9980	0.9980	0.5562
NDWI	0.3541	0.2797	0.1965	0.9020	0.7705	0.5337	0.9790	0.1655	0.9980	0.9980	
NDVI	0.9771	0.9737	0.3113	0.9743	0.8582	0.9957	0.9601	0.9973	0.5250	0.9973	
Mean	0.5203	0.4705	0.9295	0.9933	0.9064	0.9514	0.9980	0.9980	0.9980	0.9980	0.6190
Variance	0.5340	0.4673	0.4558	0.5382	0.0155	0.0053	0.0182	0.0229	0.0005	0.0259	
Homogeneity	0.7840	0.6809	0.3199	0.9927	0.0516	0.3662	0.9843	0.4601	0.9225	0.9933	
Contrast	0.4644	0.4023	0.3982	0.4644	0.0126	0.0068	0.0126	0.0162	0.0000	0.0162	
Dissimilarity	0.4728	0.7023	0.9933	0.9933	0.0235	0.3579	0.6596	0.4306	0.6320	0.9886	
Entropy	0.9888	0.4951	0.2168	0.9888	0.0791	0.1796	0.9857	0.4087	0.9234	0.9896	
ASM	0.9933	0.4908	0.2159	0.9933	0.0753	0.1726	0.9886	0.4001	0.9253	0.9933	
Correlation	0.9000	0.1080	0.0612	0.9933	0.2377	0.2129	0.9843	0.1274	0.8938	0.9927	
Mean Distance	0.5023	0.4865	0.5481	0.4705	0.9000	0.5062	0.9528	0.6007	0.8084	0.7323	

Table 5

Separability analysis of polarimetric SAR features on land-use and land-cover (LULC) pairs.

Features	J-S divergence									
	BIS-DIS	BIS-SOI	BIS-VEG	BIS-WAT	DIS-SOI	DIS-VEG	DIS-WAT	SOI-VEG	SOI-WAT	VEG-WAT
Alpha	0.1105	0.2001	0.1543	0.0848	0.1340	0.2291	0.1726	0.2621	0.2544	0.0719
Anisotropy	0.1152	0.2041	0.1094	0.8646	0.1589	0.1173	0.6971	0.1879	0.6144	0.8823
Entropy_SAR	0.0453	0.3503	0.0698	0.3470	0.4021	0.0663	0.4005	0.3899	0.1411	0.4122
Freeman_Dbl	0.3544	0.2156	0.1540	0.6564	0.3317	0.1497	0.4157	0.0884	0.2271	0.3077
Freeman_Odd	0.1968	0.7214	0.2684	0.5782	0.4132	0.0419	0.2144	0.3039	0.4886	0.1856
Freeman_Vol	0.1405	0.4224	0.1180	0.9729	0.2083	0.1060	0.9170	0.3525	0.7345	0.9632
Krogager_Kd	0.5299	0.8849	0.5897	0.9820	0.4945	0.1044	0.8571	0.2788	0.4302	0.7564
Krogager_Kh	0.2742	0.3862	0.1669	0.6024	0.0441	0.0417	0.1716	0.0929	0.0748	0.2464
Krogager_Ks	0.5645	0.4086	0.3717	0.9727	0.1591	0.1282	0.5852	0.0895	0.7031	0.6894
VanZyl3_Dbl	0.3168	0.8557	0.5078	0.8917	0.5197	0.1316	0.6263	0.2345	0.1180	0.3478
VanZyl3_Odd	0.4612	0.3449	0.2683	0.9402	0.1216	0.1126	0.4709	0.1214	0.6571	0.6328
VanZyl3_Vol	0.4612	0.7182	0.3152	0.9961	0.1682	0.0652	0.8998	0.2768	0.6221	0.9333
Yamaguchi4_Dbl	0.2303	0.1581	0.0966	0.4866	0.3595	0.2258	0.3692	0.0572	0.2531	0.2801
Yamaguchi4_Hlx	0.4903	0.6948	0.3758	0.9152	0.1158	0.0462	0.4453	0.1767	0.1627	0.4750
Yamaguchi4_Odd	0.2565	0.6135	0.3716	0.5651	0.2756	0.0580	0.2089	0.1669	0.5490	0.2655
Yamaguchi4_Vol	0.2044	0.4283	0.1278	0.9922	0.1116	0.1160	0.8805	0.2592	0.6961	0.9823
T ₁₁	0.2449	0.1584	0.1330	0.7793	0.1189	0.0858	0.4288	0.0855	0.5248	0.5529
T ₂₂	0.0967	0.3867	0.1533	0.5699	0.3644	0.0942	0.5825	0.1709	0.1133	0.3607
T ₃₃	0.2800	0.4778	0.2041	0.9221	0.0982	0.0716	0.7158	0.2335	0.4902	0.8752
Mean Distance	0.2828	0.4542	0.2398	0.7431	0.2421	0.1048	0.5294	0.2015	0.4134	0.5379

3.2. Analysis on the feature correlation

To analyze the correlation between features, Pearson Correlation of optical and SAR features was computed separately.

The correlation of optical features is demonstrated in Fig. 3(a): The Visible and NIR band features, HSV-V and Mean are all positively correlated, because they are highly related to the reflection of land surface. NDWI represents the spectrum characteristics of water, while NDVI stands for that of vegetation, so they are very much conflicted features. Entropy in GLCM grows with the increase of randomness of the grayscale distribution, and Homogeneity and ASM is large if the nearby pixels are similar, so they are highly negative correlated.

As demonstrated in Fig. 3(b), among the polarimetric SAR features, the surface scattering, double bounce scattering and volume scattering component from Freeman, Van Zyl and Yamaguchi decompositions is highly positively related. T₁₁ and surface scattering, T₂₂ and double scattering; T₃₃ and volume scattering features are highly positively related, manifesting they are features mainly related to similar scatter mechanism.

The analysis witnessed large coherent and redundant information is contained within the widely used optical and SAR features for land-use/land-cover classification.

3.3. Analysis on the contribution of single feature

In this study, the J-S distance calculated between different feature pairs are used as the indicator for separability. Features with J-S divergence larger than 0.8 are considered as with good separability.

The analysis results for optical features are summarized in Table 4. It can be observed that optical features perform well in distinguishing BIS vs. WAT, DIS vs. WAT, SOI vs. VEG, SOI vs. WAT, VEG vs. WAT since there are more than 3 feature pairs with J-S divergence higher than 0.8 (highlighted in Table 4) on these land-use pairs. However, very few optical features can effectively distinguish BIS vs. DIS and BIS vs. VEG. As for single features, NDVI, followed by Mean of correlation matrix and HSV_H are the three most important features, which could separate many land-use types effectively.

The analysis results based on J-S distance for Pol-SAR features are shown in Table 5. Generally, compared with optical features, much lower J-S divergence was obtained for all the land-use pairs. There are fewer feature pairs with J-S distance larger than 0.8 for polarimetric SAR features. Land-use pairs such as BIS-WAT, and VEG-WAT are among the better distinguished land-use pairs by SAR. As for single feature, Volume

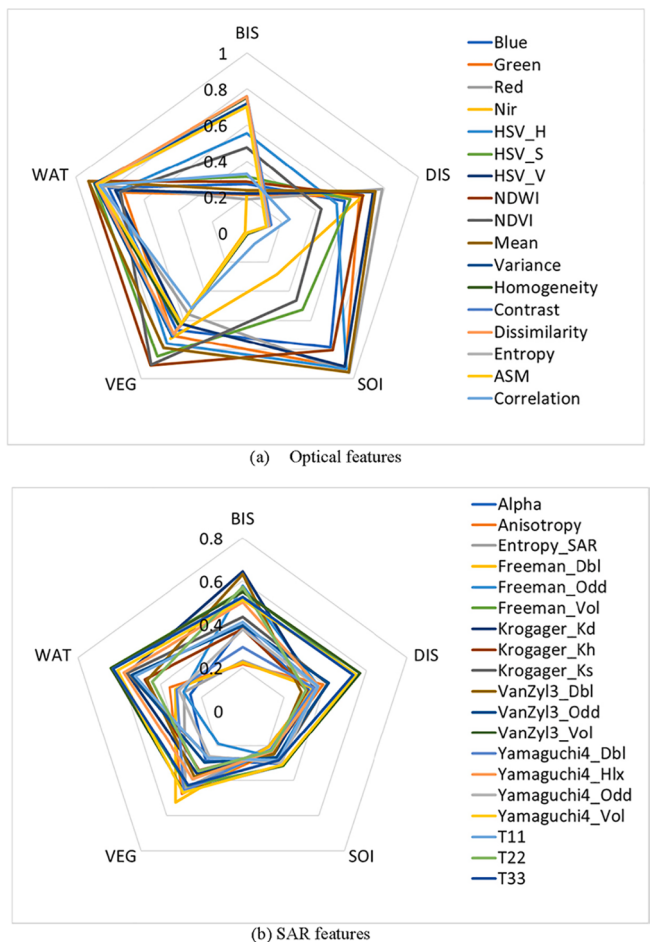


Fig. 4. Radar charts of classification accuracy on each land-use type achieved by using single features. a) optical features; b) SAR features.

scattering components (Freeman, VanZyl, Yamaguchi), Krogager_Kd and T₃₃ have strong capabilities in distinguishing WAT and other land-use types. VanZyl3_Dbl is effective in separating BIS and SOI.

Moreover, from the analysis it could be observed that some features are very import in distinguishing certain features pairs. For instances,

Table 6

Confusion matrix of land-use/land-cover classification result based on optical features (Percent).

Class	BIS (Truth)	DIS (Truth)	SOI (Truth)	VEG (Truth)	WAT (Truth)	PA
BIS	92.03	15.12	0.50	2.00	2.01	92.03
DIS	7.01	84.69	3.13	4.11	4.67	84.69
SOI	0.79	0.19	96.37	0.00	0.00	96.37
VEG	0.00	0.00	0.00	93.89	0.00	93.89
WAT	0.17	0.00	0.00	0.00	93.32	93.32
UA	89.53	69.55	95.32	100.00	99.88	

Overall Accuracy = 92.13% (46802/50802).

Kappa Coefficient = 0.8912.

Table 7

Confusion matrix of land-use/land-cover classification result based on SAR features (Percent).

Class	BIS (Truth)	DIS (Truth)	SOI (Truth)	VEG (Truth)	WAT (Truth)	PA
BIS	78.73	3.75	0.20	15.89	6.22	78.73
DIS	9.14	79.65	21.63	6.28	23.75	79.65
SOI	2.66	4.81	69.15	9.59	4.30	69.15
VEG	9.47	11.66	8.83	68.24	1.28	68.24
WAT	0.00	0.13	0.20	0.00	64.45	64.45
UA	80.80	40.47	43.91	64.81	99.90	

Overall Accuracy = 71.03% (36103/50830).

Kappa Coefficient = 0.6194.

Table 8

Confusion matrix of land-use/land-cover classification result based on feature level fusion (Percent).

Class	BIS (Truth)	DIS (Truth)	SOI (Truth)	VEG (Truth)	WAT (Truth)	PA
BIS	96.24	14.35	3.71	1.58	3.37	96.24
DIS	3.63	85.27	5.74	1.92	1.76	85.27
SOI	0.09	0.00	90.55	0.00	0.00	90.55
VEG	0.04	0.00	0.00	95.58	0.33	95.58
WAT	0.00	0.38	0.00	0.92	94.54	94.54
UA	88.24	82.18	99.50	98.86	99.56	

Overall Accuracy = 93.80% (47585/50729).

Kappa Coefficient = 0.9138.

NDVI is supportive in distinguishing BIS vs. DIS, BIS vs. SOI. Mean of GLCM is supportive in distinguishing BIS vs. VEG. Therefore, without NDVI and Mean, the aforementioned features cannot be properly distinguished.

We also calculated the mean value of J-S distance between land-use pairs to analyze their general contribution to land-use classification. For optical features, BIS-WAT is the most distinguishable land-use pairs, followed by DIS-WAT and SOI-WAT, while for SAR features, much lower separability can be obtained, and the highest separability also achieved on BIS-WAT.

In Fig. 4, the classification accuracy achieved by each feature on each land-use type is depicted. It can be seen clearly from the distribution characteristics of radar charts that the optical features have relative larger difficulties on classifying BIS and DIS, while the SAR features cannot accurately classify SOI. Hence, the need for combining optical and SAR features in the land-use type classification is preliminarily demonstrated.

3.4. Analysis on land-use classification and impervious surface extraction

Following the procedure demonstrated in section 2, urban vegetation classification was conducted by using random forest (Zhang et al., 2014; Zhang et al., 2012a). In this study, the CART(classification and

Table 9

Confusion matrix of urban vegetation extraction (Percent).

(A) Result derived by optical features			
Class	UV(Truth)	NUV(Truth)	PA
UV	93.89	0.02	93.89
NUV	6.11	99.98	99.98
UA	99.89	99.06	
(B) Result derived by SAR features			
Class	UV(Truth)	NUV(Truth)	PA
UV	68.24	5.84	68.24
NUV	31.76	94.16	94.16
UA	64.51	95.01	
(C) Result derived by fusing optical and SAR features			
Class	UV(Truth)	NUV(Truth)	PA
UV	95.58	0.17	95.58
NUV	4.42	99.83	99.83
UA	98.86	99.32	

(A) Overall Accuracy = 99.02%.

Kappa Coefficient = 0.9572.

(B) Overall Accuracy = 90.53%.

Kappa Coefficient = 0.6072.

(C) Overall Accuracy = 99.11%.

Kappa Coefficient = 0.9618.

regression tree) algorithm was applied to build the random forest. The aforementioned 17 optical and 19 SAR features were firstly applied for land-use classification separately, then all the 36 features were combined and considered for classification.

The confusion matrix of land-use classification is listed in Table 6-8. The classification accuracy and Kappa coefficient derived based on optical features is much higher than that derived from polarimetric SAR features. Based on optical features, an overall accuracy 92.13% and Kappa coefficient 0.8912 was achieved. While based on polarimetric SAR features, much lower overall accuracy and Kappa coefficient of 71.03% and 0.6164 was achieved respectively. Finally, the fusion of optical and SAR image at feature level further improved the accuracy to 93.80% and the Kappa coefficient to 0.9138.

From Table 7, it could be observed that based on polarimetric SAR features, the misclassification rate for all the land-use types increased. Especially, land-use type pairs BIS vs. VEG, DIS vs. SOI, SOI vs. VEG, DIS vs. WAT have much higher misclassification rates than classification based on optical features. The producer accuracy for DIS and SOI was very low.

In Table 8, a significant improvement of classification accuracy can be clearly observed. All land-use type pairs achieved very low misclassification rates, except for BIS and DIS (will not affect the final urban vegetation classification result). Fewer WAT was misclassified as DIS. And almost no VEG was misclassified as DIS.

Then vegetation(VEG) was extracted as urban vegetation(UV) and other land-use types were combined as non-urban vegetation(NUV). Since the mixture of land-use types within the same category e.g.: BIS and DIS, DIS and SOI will not affect the urban vegetation extraction result, the accuracy of urban vegetation extraction was higher than LULC classification. As shown in Table 9, the overall urban vegetation extraction accuracy based on optical features was 99.02%, which is much higher than the results of 90.53% achieved by SAR features. Based on fusing optical and Pol-SAR features, the urban vegetation extraction accuracy further improved and finally reached up to 99.11%. By using optical features only, the urban vegetation extraction error was resulted mainly by wrongly classified vegetation as DIS. While by fusing optical and SAR features, very little vegetation was classified as DIS, whereas more NUV was wrongly classified as urban vegetation.

The overall classification result on the study site is shown in Fig. 5. From Fig. 5a and c, very close result can be observed on classification

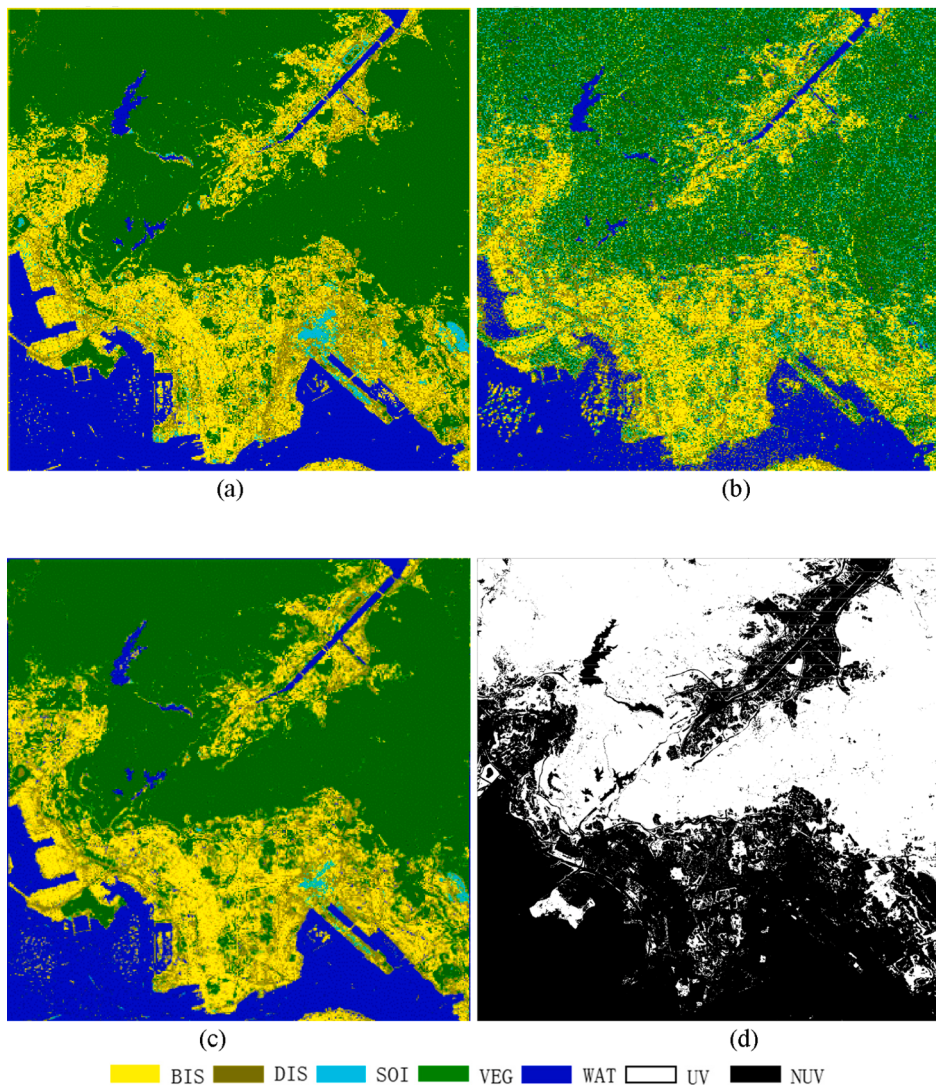


Fig. 5. Classification results: (a) land-use derived based on optical features; (b) land-use derived based on SAR features; (c) land-use derived based on feature-level fusion; (d) urban vegetation extraction result.

maps based on optical features and fusion of features. The low visual quality of the classification map of Fig. 5b is in accordance with the low classification accuracy achieved by classification based on only Pol-SAR features. In Fig. 5b, a large amount of SOI and WAT was misclassified as bare DIS, and VEG was misclassified as BIS and SOI. A large percent of DIS and VEG was also wrongly classified.

The zoomed in results of some typical regions in the study area are displayed in Fig. 6. These regions include Sha Tin, Tsing Yi, South Kowloon and Kai Tak. In the classification map derived from SAR features (column 3) many obvious misclassifications can be observed. Comparing column 1 and 3, the classification result derived by fusing optical and SAR features achieved generally similar results. Better accuracy on DIS was achieved by feature-level fusion, especially for (a) Sha Tin and (b) Tsing Yi, in which most playground and expressways were correctly classified. For (e) Kai Tak, using only optical features obtained slightly finer classification details, especially for DIS and BIS, which is probably due to the large grain effect caused by multi-look processing on SAR image. Finally, the classification map of urban vegetation is shown in Figs. 5d and 6 (UV Extraction Result).

3.5. Analysis on the number of features

In this section, analysis was conducted on the number of inputted

features for land-use classification. The classic random forest was used as the benchmark classifier and pixel accuracy was taken as the evaluation index. The contribution of each feature that derived by the random forest algorithm is ranked and listed in [Table 10](#). The contribution rates calculated by [\(15\)](#) represent the value of a single feature to the final classification performance when it is introduced into the feature set, followed the sequence of the ranking. As shown in the table, the features marked with * belong to the features extracted from SAR images, and the unmarked features belong to the features extracted from optical remote sensing images.

A five-fold cross-validation is conducted when calculating the contribution rates. The results are displayed in Table 10 from column 1 to 5. Moreover, the tested data are ranked from high to low by calculating the average values of contribution rates utilizing different features to demonstrate how much each feature contribute during classification. In the analysis, most of the optical features are ranked in higher position. Among the SAR features, the top-ranked features are: Vanzyl3_Vol, T₃₃, Freeman_Vol, Yamaguchi4_Vol, which shows again that the volume scattering component features have better classification capabilities. This result is consistent with the results of J-S divergence and single feature classification analysis.

Then the classification accuracy on the training and testing dataset achieved with the variation of feature numbers was plotted in Fig. 7. The

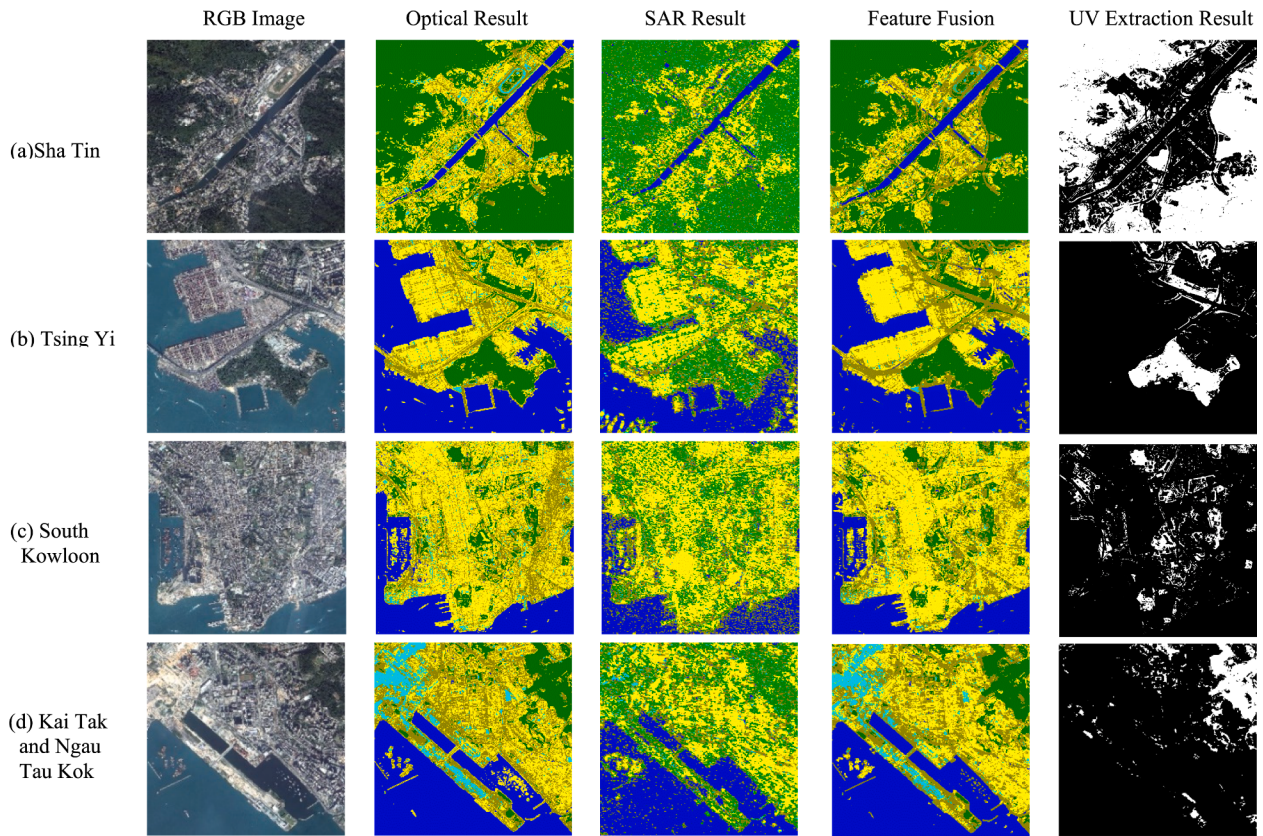


Fig. 6. Detailed classification results on various location in the study area: (a) Sha Tin; (b) Tsing Yi; (c) South Kowloon; (d) Kai Tak and Ngau Tau Kok.

classification accuracy generally grows with the increase of the number of features. When the third feature: NDWI and the eighth feature: HSV_S was brought into the feature set, significant improvement was witnessed on the accuracy curve. In Fig. 8, the classification accuracy curve of each land-use type is plotted. The accuracy curve of VEG converged first and reached a very high value, followed by BIS. SOI is relatively stable with the increase of feature numbers. The accuracy curve of WAT grows relatively slow with fluctuation initially and then reached much higher value when enough number of features were taken as input. DIS reached the lowest classification accuracy even given enough inputted features. When the third feature NDWI is input, the accuracy of VEG rises from 12.6% to 94.44%. With the increase of the number of features, the classification accuracy of VEG continues to improve, eventually reaching 95.58%. It can be seen from Fig. 8 that when the top 4 features are input, the accuracy of the vegetation category tends to be stable and the increase is slower.

4. Discussions

In this study, J-S divergence is proposed to statistically analyze the separability of features in distinguishing different types of ground targets. The analysis is high coincident with the classification results, which proves that J-S divergence is a reliable tool to quantitatively evaluate the performance of features. Land-use type pairs that can only be distinguished with fewer features and have lower average J-S distance also witnessed lower classification accuracy, such as BIS vs. DIS, BIS vs. SOI, and DIS vs. SOI.

Some key features are discovered to be crucial in the classification. Among the optical features, NDVI and NDWI that linearly irrelevant with other optical features holds the strongest capabilities in distinguishing various land-use types, demonstrating these well-designed indicators can reflect the characteristics of different ground targets well. Among the polarimetric SAR features, the volume scattering

mechanism indicators extracted from polarimetric SAR data had the largest contribution in distinguishing BIS, DIS, SOI and VEG result from the volume scattering components in these ground targets are largely different.

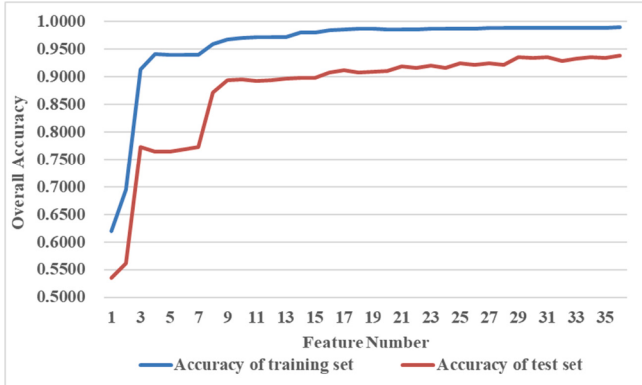
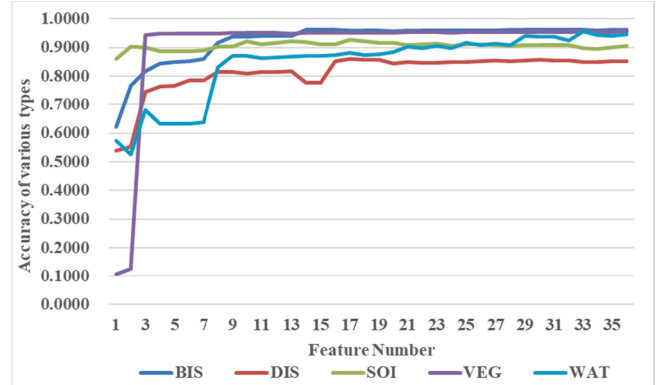
Due to different imaging mechanism between optical and SAR sensors, a large amount of complementary information can be obtained when fusing optical and SAR data. The information introduced by PolSAR features plays a key role in improving the classification accuracy. The radar chart in Fig. 4 clearly demonstrates the complementary nature of optical and polarimetric SAR features, as they have distinct advantages in the classification of land-use types. It can be observed in Table 10 that although using SAR features alone does not achieve very high classification performance, they play a very important role on improving the LULC classification accuracy in the fused features set. Polarimetric SAR features accounted for 4 positions in the top 10 contributive features. However, due to the strong characteristics of urban vegetation in optical bands, it can be well extracted by using optical image alone, leaving little room of improvement when fusing SAR features. It can be clearly observed in Fig. 8 that two optical features, namely HSV_H and NDWI, contributes most information for the classification of vegetation.

The high correlation of features from the same sensor was demonstrated by Pearson Correlation Coefficients, which results in large amount of redundant information. This fact was also confirmed in the analysis on the number of features (Figs. 7, 8) and contribution rates (Table 10). The classification accuracy does not largely increase when sufficient number of features are inputted. This phenomenon is called “curse of dimensionality” and has been well discussed in some studies (Gambardella et al., 2010). Therefore, in practice a subset of the introduced features, e.g. the top 10 optical and SAR features in this study case, is taken to balance the classification accuracy and training difficulty.

Table 10

Contribution rates of features.

Contribution Analysis	Contribution Rates						
Features	1	2	3	4	5	Average	Ranking
HSV_H	0.1750	0.1320	0.0790	0.1350	0.1260	0.1294	1
Freeman_Vol*	0.0780	0.0310	0.0830	0.0650	0.1520	0.0818	2
NDWI	0.0640	0.0750	0.0800	0.0570	0.1260	0.0804	3
NDVI	0.1240	0.0570	0.0900	0.1000	0.0220	0.0786	4
VanZyl3_Vol*	0.0300	0.0830	0.0860	0.1370	0.0560	0.0784	5
Yamaguchi4_Vol*	0.1020	0.0470	0.0840	0.0660	0.0480	0.0694	6
T ₃₃ *	0.0580	0.0830	0.0240	0.0350	0.0660	0.0532	7
HSV_S	0.0500	0.0510	0.0280	0.0780	0.0240	0.0462	8
Mean	0.0200	0.0400	0.0400	0.0510	0.0460	0.0394	9
Nir	0.0270	0.0590	0.0320	0.0150	0.0200	0.0306	10
Freeman_Dbl*	0.0330	0.0220	0.0400	0.0290	0.0240	0.0296	11
Red	0.0120	0.0220	0.0500	0.0080	0.0230	0.0230	12
Contrast	0.0130	0.0030	0.0270	0.0230	0.0490	0.0230	13
Yamaguchi4_Dbl*	0.0180	0.0250	0.0200	0.0260	0.0260	0.0230	14
HSV_V	0.0250	0.0120	0.0220	0.0290	0.0210	0.0218	15
Krogager_Kd*	0.0220	0.0300	0.0250	0.0120	0.0180	0.0214	16
Variance	0.0040	0.0300	0.0200	0.0220	0.0050	0.0162	17
VanZyl3_Dbl*	0.0210	0.0260	0.0090	0.0080	0.0140	0.0156	18
Green	0.0030	0.0270	0.0020	0.0070	0.0230	0.0124	19
Dissimilarity	0.0060	0.0300	0.0090	0.0130	0.0030	0.0122	20
Entropy	0.0180	0.0080	0.0250	0.0010	0.0040	0.0112	21
Yamaguchi4_Hlx*	0.0030	0.0260	0.0090	0.0020	0.0130	0.0106	22
Krogager_Ks*	0.0090	0.0150	0.0120	0.0070	0.0090	0.0104	23
Alpha*	0.0060	0.0100	0.0150	0.0080	0.0110	0.0100	24
VanZyl3_Odd*	0.0040	0.0050	0.0130	0.0100	0.0180	0.0100	25
Blue	0.0050	0.0040	0.0230	0.0070	0.0100	0.0098	26
Anisotropy*	0.0170	0.0090	0.0040	0.0120	0.0020	0.0088	27
T ₁₁ *	0.0050	0.0170	0.0070	0.0020	0.0090	0.0080	28
ASM	0.0230	0.0000	0.0030	0.0080	0.0030	0.0074	29
Freeman_Odd*	0.0070	0.0050	0.0060	0.0090	0.0040	0.0062	30
Yamaguchi4_Odd*	0.0080	0.0040	0.0080	0.0060	0.0030	0.0058	31
T ₂₂ *	0.0020	0.0040	0.0040	0.0020	0.0120	0.0048	32
Homogeneity	0.0030	0.0020	0.0010	0.0060	0.0070	0.0038	33
Krogager_Kh*	0.0020	0.0020	0.0080	0.0020	0.0010	0.0030	34
Correlation	0.0010	0.0000	0.0110	0.0010	0.0010	0.0028	35
Entropy_SAR*	0.0020	0.0020	0.0030	0.0020	0.0010	0.0020	36

**Fig. 7.** Overall classification accuracy variance with different number of input features.**Fig. 8.** Classification accuracy on each land-use type with growing number of input features.

5. Conclusion

In this paper, comprehensive analysis was conducted on the key factors of urban vegetation extraction by fusing high resolution optical and SAR data. The main outcome can be summarized as follows:

- (1) A framework was proposed to analysis features from multi-source remote sensing images for land-use classification and urban vegetation extraction. The analysis result derived in each parts coincides with each other.

- (2) Optical and Pol-SAR data carries valuable complementary information in the classification of different types of ground targets. Through the analysis how the fusing of optical and Pol-SAR information improves the LULC classification and is demonstrated.
- (3) Some key features such as NDVI and Mean value of GLCM carry distinct information for discriminating certain land-use types, which needs especial consideration for improving the land-use classification performance.
- (4) Among SAR features, volume components from polarization decompositions have larger contribution in distinguishing various land-use types.

- (5) Optical features contribute most information for urban vegetation extraction while little improvement is obtained by introducing polarimetric SAR features.
- (6) When fusing the optical and SAR features, the classification accuracy does not grow significantly after several features are taken. Therefore, in practice a feature set with a certain number of features is a proper choice for balancing the performance and efficiency.

In recent years, the availability of earth observation data from high resolution optical sensors and advanced SAR sensors provides valuable information for urban remote sensing. The development of the land-use/land-cover classification technology enables scientists to monitor the changes of urban land-cover frequently, precisely, and easily, which will surely benefit studies related to urban environment, society, and economy. This study is concentrated on the contribution and interactions of features obtained by optical and SAR sensors. By taken advantage of the knowledge discovered in this study, algorithms can be designed to achieve better and more robust result on LULC classification and urban vegetation extraction. Further analysis will be conducted on other study regions, to further verify the analysis results and test the generalization performance of the proposed classification algorithm.

Funding Information

This work was supported in part by the National Key Research and Development Program of China (2016YFB0501501), Scientific Research Project of Beijing Educational Committee (KM202110005024) and the Natural Science Foundation of China (41706201).

CRediT authorship contribution statement

Yunkun Bai: Data curation, Writing - original draft, Software. **Guangmin Sun:** Funding acquisition, Supervision. **Yu Li:** Conceptualization, Methodology, Writing - review & editing. **Peifeng Ma:** Software, Validation. **Gang Li:** . **Yuanzhi Zhang:** Funding acquisition, Supervision, Writing - review & editing.

Declaration of Competing Interest

The authors declare that they have no known competing financial interests or personal relationships that could have appeared to influence the work reported in this paper.

References

- Bhattacharya, A., Touzi, R., 2011. Polarimetric SAR urban classification using the Touzi target scattering decomposition. *Canadian Journal of Remote Sensing* 37 (4), 323–332.
- Chen, J., Quegan, S., Yin, X., 2011. Calibration of spaceborne linearly polarized low frequency SAR using polarimetric selective radar calibrators. *Progress In Electromagnetics Research* 114, 89–111.
- Cloude, S.R., Pottier, E., 1997. An entropy based classification scheme for land applications of polarimetric SAR. *IEEE transactions on geoscience and remote sensing* 35 (1), 68–78.
- Dare, P.M., 2005. Shadow analysis in high-resolution satellite imagery of urban areas. *Photogrammetric Engineering & Remote Sensing* 71 (2), 169–177.
- Deng, C., Wu, C., 2012. BCI: A biophysical composition index for remote sensing of urban environments. *Remote Sensing of Environment* 127, 247–259.
- Freeman, A., Durden, S.L., 1998. A three-component scattering model for polarimetric SAR data. *IEEE transactions on geoscience and remote sensing* 36 (3), 963–973.
- Gambardella, A., Giacinto, G., Migliaccio, M., Montali, A., 2010. One-class classification for oil spill detection. *Pattern Analysis & Applications* 13 (3), 349–366.
- Henderson, F.M., Xia, Z.G., 1997. SAR applications in human settlement detection, population estimation and urban land use pattern analysis: a status report. *IEEE transactions on geoscience and remote sensing* 35 (1), 79–85.
- Krogager, E., 1990. New decomposition of the radar target scattering matrix. *Electronics Letters* 26 (18), 1525–1527.
- Kang, Y., Zhang, F., Gao, S., Lin, H., Liu, Y., 2020. A review of urban physical environment sensing using street view imagery in public health studies. *Annals of GIS* 26 (3), 261–275.
- Kuang, W., Dou, Y., 2020. Investigating the Patterns and Dynamics of Urban Green Space in China's 70 Major Cities Using Satellite Remote Sensing. *Remote Sensing* 12 (12), 1929.
- Lee, J.S., Pottier, E., 2017. Polarimetric radar imaging: from basics to applications. CRC Press.
- Li, Y., Zhang, Y., Chen, J., Zhang, H., 2013. Improved compact polarimetric SAR quad-pol reconstruction algorithm for oil spill detection. *IEEE geoscience and remote sensing letters* 11 (6), 1139–1142.
- Lim, T.S., Loh, W.Y., Shih, Y.S., 2000. A comparison of prediction accuracy, complexity, and training time of thirty-three old and new classification algorithms. *Machine learning* 40 (3), 203–228.
- Lu, D., Weng, Q., 2006. Use of impervious surface in urban land-use classification. *Remote Sensing of Environment* 102 (1–2), 146–160.
- Migliaccio, Mascolo, Nunziata, Sarti, & Mazzarella (2014). COSMO-SkyMed HH/VV PingPong Mode SAR Data to Discriminate Among Sea, Urban, and Vegetated Areas. *IEEE Journal of Selected Topics in Applied Earth Observations and Remote Sensing*, vol.7, no.7, pp.2880-289.
- Ridd, M. K. (1995). Exploring a VIS (vegetation-impervious surface-soil) model for urban ecosystem analysis through remote sensing: comparative anatomy for cities. *International journal of remote sensing*, 16(12), 2165-2185.[4].
- Rokach, L., 2010. Ensemble-based classifiers. *Artificial intelligence review* 33 (1), 1–39.
- Schmitt, M., Zhu, X.X., 2016. Data fusion and remote sensing: An ever-growing relationship. *IEEE Geoscience and Remote Sensing Magazine* 4 (4), 6–23.
- Salentinig, A., Gamba, P., 2015. Combining SAR-based and multispectral-based extractions to map urban areas at multiple spatial resolutions. *IEEE Geoscience and Remote Sensing Magazine* 3 (3), 100–112.
- Shao, Z., Fu, H., Fu, P., Yin, L., 2016. Mapping urban impervious surface by fusing optical and SAR data at the decision level. *Remote Sensing* 8 (11), 945.
- Van Zyl, J. J., Arii, M., & Kim, Y. (2008, June). Requirements for model-based polarimetric decompositions. In 7th European Conference on Synthetic Aperture Radar (pp. 1–4). VDE.
- Weng, Q., Hu, X., Lu, D., 2008. Extracting impervious surfaces from medium spatial resolution multispectral and hyperspectral imagery: a comparison. *International Journal of Remote Sensing* 29 (11), 3209–3232.
- Wu, C., Murray, A.T., 2003. Estimating impervious surface distribution by spectral mixture analysis. *Remote sensing of Environment* 84 (4), 493–505.
- Yamaguchi, Y., Moriyama, T., Ishido, M., Yamada, H., 2005. Four-component scattering model for polarimetric SAR image decomposition. *IEEE Transactions on Geoscience and Remote Sensing* 43 (8), 1699–1706.
- Zhang, F., Zhou, B., Liu, L., Liu, Y., Fung, H.H., Lin, H., Ratti, C., 2018a. Measuring human perceptions of a large-scale urban region using machine learning. *Landscape and Urban Planning* 180, 148–160.
- Zhang, H., Lin, H., Zhang, Y., Weng, Q., 2015. Remote sensing of impervious surfaces in tropical and subtropical areas, Vol. 11. CRC Press.
- Zhang, H., Lin, H., Wang, Y., 2018b. A new scheme for urban impervious surface classification from SAR images. *ISPRS Journal of Photogrammetry and Remote Sensing* 139, 103–118.
- Zhang, H., Zhang, Y., Lin, H., 2012a. A comparison study of impervious surfaces estimation using optical and SAR remote sensing images. *International Journal of Applied Earth Observation and Geoinformation* 18, 148–156.
- Zhang, Y., Lin, H., Liu, Q., Hu, J., Li, X., Yeung, K., 2012b. Oil-spill monitoring in the coastal waters of Hong Kong and vicinity. *Marine Geodesy* 35 (1), 93–106.
- Zhang, Y., Zhang, H., Lin, H., 2014. Improving the impervious surface estimation with combined use of optical and SAR remote sensing images. *Remote Sensing of Environment* 141, 155–167.
- Zhang, Y., Li, Y., Liang, X.S., Tsou, J., 2017. Comparison of oil spill classifications using fully and compact polarimetric SAR images. *Applied Sciences* 7 (2), 193.